On the role of solute drag in reconciling laboratory and natural constraints on olivine grain growth kinetics

Jean Furstoss, Carole Petit, Andrea Tommasi, Clément Ganino, Daniel Pino Muñoz, Marc Bernacki

Author copy of the final (peer-reviewed) version
Article published in Geophysical Journal International in November 2020
Please reference to: Furtoss, J., Petit, C., Tommasi, A., Ganino, C., Piño-Munoz, D. Bernacki, M. (2020) On the role of solute drag in reconciling laboratory and natural constraints on olivine grain growth kinetics. Geophys. J. Intern., doi : 10.1093/gji/ggaa520.

On the role of solute drag in reconciling laboratory and natural constraints on olivine grain growth kinetics

Jean Furstoss[1, 2*], Carole Petit[1], Andrea Tommasi[3], Clément Ganino[1], Daniel Pino Muñoz[2], Marc Bernacki[2]

[1] *Université Nice Côte d'Azur, CNRS, OCA, IRD, Géoazur, France*
[2] *MINES ParisTech, PSL Research University, CEMEF-Centre de mise en forme des matériaux, CNRS UMR 7635, France*
[3] *Geosciences Montpellier, CNRS & Université de Montpellier, Montpellier, France*
*__Contact__: furstoss@geoazur.unice.fr

Abstract

We investigate the effect of solute drag on the grain growth (GG) kinetics in olivine-rich rocks through full field and mean field modelling. Considering a drag force exerted by impurities on grain boundary migration allows reconciling laboratory and natural constraints on olivine GG kinetics. Solute drag is implemented in a full field level-set framework and in a mean field model that explicitly accounts for a grain size distribution. After calibration of the mean field model on full field results, both models are able to both reproduce laboratory GG kinetics and predict grain sizes consistent with observations in peridotite xenoliths from different geological contexts.

Keywords : Microstructure, numerical modelling, mantle processes

1 Introduction

Olivine is the major constituent of the Earth upper mantle, and its grain growth (GG) kinetics is of major importance in several geodynamic processes. In fact, a variation in the mean grain size of a mantle rock may drastically change its mechanical behavior through the grain size dependence of the diffusion creep

regime (Karato et al., 1986). In this regime, the rock strength is inversely proportional to the grain size to a power p, with p = 2 (Karato et al., 1986). Moreover grain growth may lead the rocks into the grain-size independent, but stress-dependent dislocation creep regime. A variation in the mean grain size of olivine rocks may therefore produce marked changes in the upper mantle rheology, which may control strain localization (Braun et al., 1999). Consistently, preservation of small grain sizes (mylonitic or ultramylonitic microstructures within ductile shear zones (Vissers et al., 1991)) has been proposed as one of the mechanisms allowing to preserve weak plate boundaries over geological times (Bercovici and Ricard, 2014).

However, numerical models of grain growth without stored energy (Furstoss et al., 2018; Chu and Korenaga, 2012) based on experimental data on olivine GG (Karato, 1989; Ohuchi and Nakamura, 2007; Hiraga et al., 2010) speak against the persistence of small grain sizes through million years in pure olivine rocks. These models simulate well the experimental data, but they fail even to predict the commonly observed plurimillimetric grain sizes observed in dunites when run on geologically relevant timescales (i.e., over millions of years), for which they predict meter scale grain sizes (Furstoss et al., 2018; Chu and Korenaga, 2012). To obtain a GG kinetics compatible with natural observations in upper mantle rocks, the presence of second phases is often considered (Hiraga et al., 2010; Furstoss et al., 2020). Nevertheless, to preserve very small olivine grain sizes ($<< 100\mu m$) over millions of years, these models have to introduce some questionable features to increase the impediment of olivine grain boundary migration (GBM), such as very slow GG of the second phases (Nakakoji and Hiraga, 2018), grain size reduction of all phases and enhanced mixing between phases (Bercovici and Ricard, 2012) or the presence of small fixed particles (Furstoss et al., 2020) .

Our understanding of olivine GG in itself is limited by the inconsistency between laboratory and natural time and spatial scales. All GG models are calibrated on experimental data obtained for ultra-fine grains (1 to $30\mu m$), for which the grain size evolution is measurable at experimental timescales (a few hours to several days), and then extrapolated to natural conditions. As a consequence, if a physical mechanism becomes prominent only for grain sizes larger than $50\mu m$, its effect will not be captured in the experiments. An example of such a physical mechanism is the drag force exerted by impurities also called solute drag, which has been very seldom considered in studying GG in rocks (orthopyroxene (Skemer and Karato, 2007), halite (Guillope and Poirier, 1979)) and never accounted for modeling GG of olivine.

In the present work we tested the effect of solute drag on the GG kinetics of olivine. We performed 2D full field GG simulations using a level-set (LS) framework (Bernacki et al., 2011) in which we implemented the solute drag effect. These models show that considering this mechanism allows for consistent simulation of olivine GG kinetics at both experimental and upper mantle conditions. We then adjust a mean-field model on results of the full field simulations to propose an analytical expression allowing to compute efficiently the grain size evolution within geodynamic large scale models accounting for grain size-dependent rheologies.

2 Modeling solute drag

Impurities present within the crystal lattice and segregated at grain boundaries can have an impact on their migration kinetics through the so called solute drag effect. The grain boundary migration velocity (v) is generally expressed as (Humphreys and Hatherly, 2012) :

$$v = MP, \tag{1}$$

where $M(m^4.J^{-1}.s^{-1})$ is the grain boundary mobility and P is the sum of the pressures exerted on the grain boundary. The solute drag effect can be described in terms of drag pressure exerted on the grain boundary, which is a function of the grain boundary velocity and impurities concentration and nature. This drag pressure has been quantified theoretically (Lücke and Detert, 1957) . Its intensity follows three main regimes (high, intermediate and low velocity), similarly to dislocation impediment by Cottrell atmospheres (Cottrell and Bilby, 1949). Impurities segregated around the grain boundary interact with it and when the grain boundary migrates, the impurity cloud tends to accompany it. In the high velocity regime, the grain boundary moves so fast that the segregated impurities cannot follow the interface and the interactions between the impurities and the grain boundary are strongly reduced. In the low velocity regime, the impurity cloud stays segregated around the moving grain boundary, but the intrinsic drag of the grain boundary due to the intrinsic defects within the interface is generally higher than the drag exerted by the impurities (Fig.1). Between these two regimes, an intermediate regime exists where the impact of solute drag on GBM is important.

Even if the drag effect is expected to follow different mathematical relationships depending on the velocity regime (Lücke and Detert, 1957), an unified expression for the drag pressure P_i exerted by a c_0 concentration of impurities (within the bulk) valid for the three regimes has been proposed by Cahn (1962) :

$$P_i = \frac{\alpha v c_0}{1 + \beta^2 v^2}, \tag{2}$$

where v is the grain boundary velocity norm, c_0 the concentration of im-

purities within the bulk, and $\alpha(J.s.m^{-4})$ and $\beta(s.m^{-1})$ are two parameters modulating the intensity of the solute drag. α controls the intensity of the solute drag pressure and β constrains the grain boundary velocity which is the most impacted by the presence of the impurities (Fig.1). The solute drag effect is most effective for grain boundary velocities close to $1/\beta$.

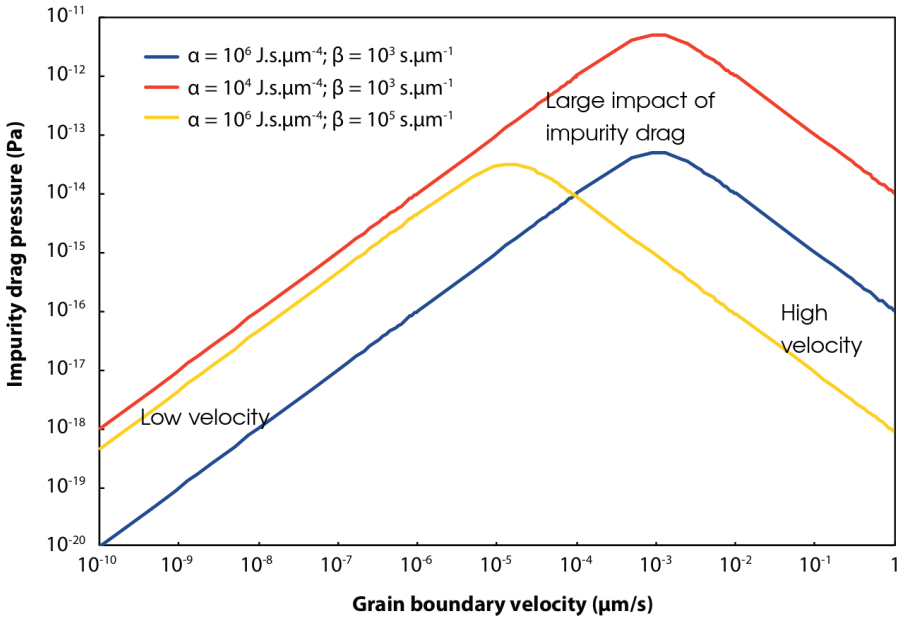

Figure 1: Solute drag pressure intensity as a function of the grain boundary velocity calculated using eq.2 for $c_0 = 100$ppm and different values of α and β.

The α and β parameters can be expressed as integrals of functions $D(x)$ and $E(x)$ representing the variation of the impurity diffusion coefficient and of the interaction energy, respectively, along the grain boundary normal (x). As these two functions are difficult to constrain experimentally, their mathematical expressions are generally hypothesized in an integrable way, which permits to obtain analytical expressions for α and β (Cahn, 1962) :

$$\alpha = \frac{N_v (k_b T)^2}{E_0 D} (sinh(\frac{E_0}{k_b T}) - \frac{E_0}{k_b T}), \tag{3}$$

and,

$$\beta^2 = \frac{\alpha k_b T \delta}{2 N_v E_0^2 D}, \tag{4}$$

where $N_v(m^{-3})$ is the number of atoms per unit volum, k_b the Boltzmann constant, $E_0(J)$ the interaction energy, $D(m^2.s^{-1})$ the diffusion coefficient of the impurity within the bulk and $\delta(m)$ is the characteristic segregation length of the impurities around the grain boundary.

2.1 Semi-explicit implementation of solute drag within the level-set framework

The LS framework (Bernacki et al., 2009), already used to model olivine GG (Furstoss et al., 2018, 2020), proposes an implicit description of the polycrystal through the use of LS functions representing the signed distance function to the grain boundaries surrounding the grain they represent (positive inside the grain and negative elsewhere) in a finite element (FE) context. The microstructural evolution is simulated by moving the LS functions according to physical laws describing GBM (Cruz-Fabiano et al., 2014) or by creating LS functions to represent new grains nucleated during the recrystallization mechanisms (Maire et al., 2017). Theoretically, each grain of a polycrystal is represented by its own LS function. However to reduce the computation time and memory storage, several non-neighboring grains in the initial microstructure can be grouped to form Global Level Set (GLS) functions thanks to a graph coloration technique. Re-coloration is then used to avoid numerical grain coalescence during grain boundary motion (Scholtes et al., 2015, 2016). The GLS functions dis-

placement is computed within an efficient FE framework (Scholtes et al., 2015; Shakoor et al., 2015) using anisotropic mesh refinement around interfaces (Resk et al., 2009). The initial microstructure is generated using a Voronoï-Laguerre Dense Sphere Packing algorithm (Hitti et al., 2012), which respects precisely an imposed initial grain size distribution.

If GG is solely controlled by capillarity (reduction in the grain boundary energy) and solute drag, the grain boundary velocity is controlled by the difference between the capillarity pressure (P_{capi}) and solute drag pressure (P_i described by Eq.2) as :

$$\vec{v} = M(P_{capi} - P_i)\vec{n} = M(-\gamma\kappa - \frac{\alpha c_0 v}{1+\beta^2 v^2})\vec{n}, \tag{5}$$

where $M(m^4.J^{-1}.s^{-1})$ and $\gamma(J.m^{-2})$ are the grain boundary mobility and energy respectively, κ is the grain boundary local curvature (in 2D) or the sum of the main local curvatures (in 3D) and $\vec{n}$ the outward unit normal to the grain boundary.

By introducing the GLS function Φ_i to represent the grains i, we can obtain the following implicit and explicit first order time discretizations for the temporal derivative of Φ_i :

$$\frac{\partial \Phi_i}{\partial t} = \frac{\Phi^{t+\Delta t} - \Phi^t}{\Delta t}, \tag{6}$$

for the GLS function velocity :

$$v = \frac{\Phi^{t+\Delta t} - \Phi^t}{\Delta t}, \tag{7}$$

and for the squared velocity :

$$v^2 = (\frac{\Phi^t - \Phi^{t-\Delta t}}{\Delta t})^2 = v_{old}^2. \tag{8}$$

The displacement of the GLS functions is computed using the convective LS equation (Osher and Sethian, 1988) :

$$\frac{\partial \Phi_i}{\partial t} + \vec{v} \cdot \vec{\nabla} \Phi_i = 0. \tag{9}$$

Considering the geometrical properties of LS function $\kappa = -\Delta\Phi$, $\vec{\nabla}\Phi.\vec{\nabla}\Phi = 1$, $\vec{\nabla}\Phi = -\vec{n}$, using the above time discretization and substituting Eq.5 within the above convective LS equation, we obtain the FE strong formulation :

$$\mathcal{M}\frac{\Phi^{t+\Delta t}}{\Delta t} - M\gamma\Delta\Phi^{t+\Delta t} = \mathcal{M}\frac{\Phi^{t}}{\Delta t}, \tag{10}$$

where :

$$\mathcal{M} = 1 + \frac{M\alpha c_0}{1+\beta^2 v_{old}^2}. \tag{11}$$

The fact that Eq.11 uses v_{old}^2 instead of v^2 is a simplification that reduces the non-linear behaviour of the problem. In practical terms, the time marching scheme uses a small timestep, thus the error of replacing v^2 by v_{old}^2 is small and this greatly simplifies the numerical scheme allowing its implementation in a generic FE code. This formulation is similar to the diffusion formulation classically used for capillarity driven GG in the LS formalism (Cruz-Fabiano et al., 2014). By analogy with the heat diffusion equation, $\mathcal{M}$ is equivalent to a mass term (i.e. the product between the specific heat capacity and density). The main difference relative to the classic LS approach for capillarity-driven GG is that when solute drag is modelled the mass term differs from one and depends on the velocity of the LS function at time $t - \Delta t$. This heterogeneous mass term is computed on each node of the mesh and linearly interpolated.

A major drawback of the LS approach lies in the fact that during grain boundary migration, the GLS are no longer distance functions $||\vec{\nabla}\phi|| \neq 1$. This is par-

ticularly problematic when a remeshing technique depending on the distance property is used at grain interfaces. In addition, the new diffusive formulation proposed in Eq.10 requires a distance function as it is based on the respect of $||\vec{\nabla}\phi|| = 1$, at least in a thin layer around the interface. For these reasons, the GLS functions need to be reinitialized at each time step in order to restore their metric property. Numerous approaches exist for this reinitialization procedure. Here we use a fast and accurate approach usable in unstructured FE mesh proposed by Shakoor et al. (2015). The residual errors inherent to this approach are discussed in (Florez et al., 2020).

The introduction of the solute drag pressure is expected to reduce the GG kinetics. Thus, its influence has to be accounted for in the adaptative time stepping scheme to allow larger steps when the grain size evolves slowly. The timestep is computed by imposing a maximal incremental displacement corresponding to a given fraction (H) of the LS reinitialized width (E_p) :

$$\Delta t = \frac{H E_p}{v_m}, \tag{12}$$

where v_m is the grain boundary mean velocity :

$$v_m = M(\frac{\gamma}{\bar{R}} - \frac{c_0 \alpha |\bar{\dot{R}}|}{1 + \beta^2 \bar{\dot{R}}^2}), \tag{13}$$

where $\bar{R}$ and $\bar{\dot{R}}$ are the mean grain radius and its temporal evolution, respectively. To avoid negative timestep values, we impose a lower bound for v_m at $M\gamma/R_{max}$, where R_{max} is the maximum grain radius.

The explicit time discretization in Eq.8 may have an impact on the numerical resolution if the non-linearity of the grain boundary velocity (Eq.5) is strong. This has been evaluated by performing computations with different timesteps (Fig.2), which show that mean grain size evolution does not depend on H,

neither for the reference case without solute drag ($\mathcal{M} = 1$), nor for the case with solute drag. Thus, the strong formulation (Eq.10) for the displacement of LS functions accounting for solute drag can be validated. When accounting for solute drag by impurities, the GG kinetics follows the expected trend and is much slower than in cases without drag (Fig.2).

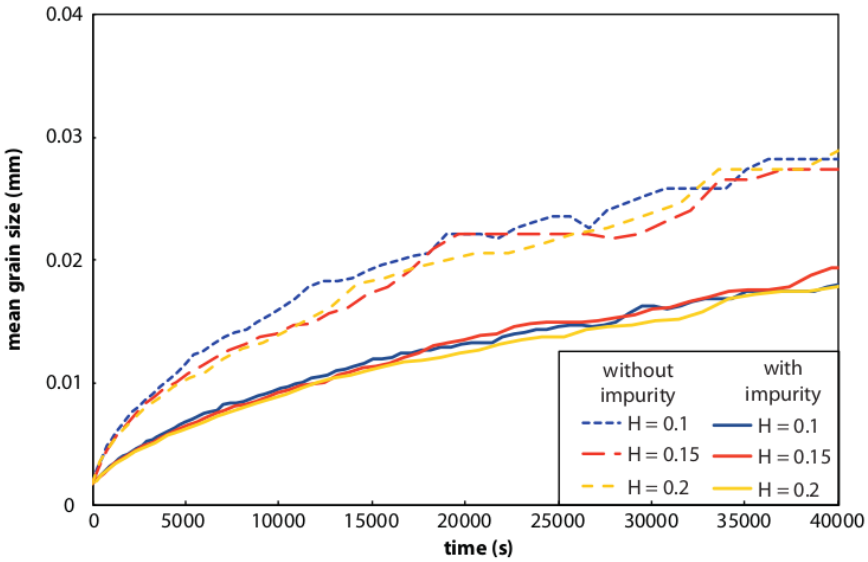

Figure 2: Full field model of the mean grain radius evolution using $M = 2.9 \cdot 10^{-2} mm^4.J^{-1}.s^{-1}$, $\gamma = 10^{-6} J.mm^{-2}$ (representing olivine material parameters at 1573K from (Furstoss et al., 2020)) for a case without impurities (dashed lines) and for a case with $c_0 = 1000ppm$, $\alpha = 10^5 J.s.mm^{-4}$ and $\beta = 10^5 s.mm^{-1}$ (solid lines). The H coefficient controls the timestep (Eq.12).

2.2 Mean field approach for GG with solute drag

To construct a mean field model describing GG kinetics including solute drag, it is important to account for the grain size distribution. Computing GG kinetics using only the mean grain size evolution will hide the dispersion of the solute drag pressures exerted within the microstructure due to variations in the

capillarity force, which is a function of grain size. This will result in three clear stages of grain size evolution as illustrated in Fig.1 : an initial mean grain size evolution unimpacted by solute drag (high velocity regime), a second phase, the most impacted by solute drag, where the mean grain size will be quasi-static and a final phase also unimpacted by solute drag (low velocity regime). To account for the coexistence of these three regimes within the microstructure and predict realistic mean grain size evolutions, the initial dispersion of individual grain sizes and their evolution rates have to be considered.

For this purpose, we adapted the (Hillert, 1965) model, which proposes a discrete representation of the grain size distribution (GSD) in the microstructure. By considering R_i the radius of the i-grain size bin, the Hillert's model allows computing the evolution of each bin by accounting for the capillarity pressure expressed as $M\gamma\kappa\frac{\overline{R}^2}{\overline{R^2}}(\frac{\overline{R}}{\overline{R^2}} - \frac{1}{R_i})$, with $\kappa \approx 1.6$ from (Maire et al., 2016). This procedure enables to follow the evolution of each bin of the initial GSD. This mean field approach is able to reproduce, in terms of GSD, the predictions of full field simulations in context of pure GG in 2D (Cruz-Fabiano et al., 2014) and in 3D (Maire et al., 2016) even for complex initial GSD (like bimodal ones). To account for solute drag, we subtract from the capillarity pressure the solute drag pressure (Eq.2) replacing v by $\dot{R}_i$ and v^2 by $\dot{R}^2_{i,old}$ (i.e. the grain size evolution rate at the precedent increment), which gives :

$$\dot{R}_i = \kappa\frac{\overline{R}^2}{\overline{R^2}}M(\gamma(\frac{\overline{R}}{\overline{R^2}} - \frac{1}{R_i}) - \frac{\alpha c_0 \dot{R}_i}{1+\beta^2\dot{R}^2_{i,old}}), \tag{14}$$

which can be reformulated as :

$$\dot{R}_i = \gamma(\frac{\overline{R}}{\overline{R^2}} - \frac{1}{R_i})/(\frac{\overline{R^2}}{M\kappa\overline{R}^2} + \frac{\alpha c_0}{1+\beta^2\dot{R}^2_{i,old}}), \tag{15}$$

To account for topological effects or a non-uniform mass term along grain bound-

aries, equation 15 is generalized through the following expression :

$$\dot{R}_i = \gamma(\frac{\overline{R}}{\overline{R^2}} - \frac{1}{R_i})/(\frac{\overline{R^2}}{M\kappa\overline{R}^2} + \frac{C_\alpha \alpha c_0 \dot{R}^n_{i,old}}{1 + (C_\beta\beta)^2 \dot{R}^2_{i,old}}), \tag{16}$$

where C_α, C_β and n are mean field parameters which have to be calibrated on full field simulations. It can be noticed that the equation 16 is equivalent to the non-generalized form (Eq.15) for $n = 0$ and $C_\alpha = C_\beta = 1$.

In practice, each bin R_i are equipropables in number. We begin with a list of bins generated from an imposed initial GSD and compute iteratively their evolutions. If the grain radius of a bin becomes lower than $0.1\mu m$ it is considered as consumed by the growth of neighboring grains and removed from the bin list. As this mean field model is intended to be used for long term calculations (Myr), the initial number of bins needed to preserve a representative number of bins after long annealing time is very large and the computational cost becomes prohibitive. Thus, we use a repopulation strategy allowing to do the calculation with a reasonable number of bins all along the simulation. To do so, when the number of bins is less than a minimal number, we repopulate the bin list by adding ten new bins for each existing bin R_i with radii ranging between $0.9R_i$ and $1.1R_i$ with a step of $0.02R_i$. Those range of values have been chosen in order to minimize the difference between GSD before and after repopulation step (see an example in Fig.3). The minimal number of bins is fixed at 40 based on a convergence study.

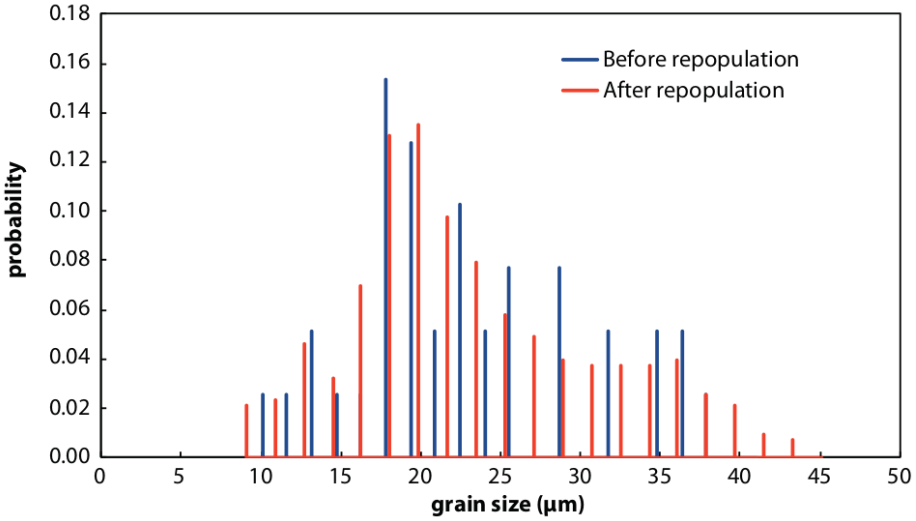

Figure 3: Example of GSD (in number) before and after a repopulation step with a minimal bin number of 40. Both histograms are constructed using 20 classes ranging between the radii of the bins with the minimal and maximal grain radius.

3 Solute drag in olivine

In mantle rocks, several incompatible elements and impurities are present in concentrations ranging from few to hundreds *ppm* (De Hoog et al., 2010). Some of them are more or less homogeneously dispersed through the bulk material, but others can be enriched at grain boundaries (Suzuki, 1987). The elements that can influence grain growth through solute drag are those that exhibit a partitioning between grain interiors and boundaries. The major constituent of mantle rocks is olivine, an orthorhombic material of composition $(Fe, Mg)_2SiO_4$. In olivine-rich rocks, chromium (Cr), aluminum (Al) and calcium (Ca) (Suzuki, 1987; Hiraga et al., 2003, 2004) display a strong partitioning between olivine grain matrix and boundaries, the latter being often qualified as «incompatible

element reservoirs ». The major parameters controlling their effect on GBM are the element concentration, diffusion coefficient and interaction energy with grain boundary. The latter will control at first order the intensity of the drag pressure exerted by the impurity. As interstitials, vacancies and even grain boundaries could have a non-null electrical charge in materials as olivine, the full formulation of this energy term should include, in addition to an elastic part, an electrostatic component. However for sake of simplicity we will assume a pure elastic interaction corresponding to the lattice distortion due to the misfit between the impurity size and the size of the typical host ion the impurity replaces. Close to and within olivine grain boundaries the impurities may replace Mg ions (a depletion in Mg is observed at grain boundaries) (Hiraga et al., 2004). Within the grain interiors, Mg ions are located in the octahedral M sites, and the interaction energy between impurity and grain boundary can be computed, as a first order approximation, using the characteristic length r_0 of those sites (Hiraga et al., 2004) :

$$E_0 = 4\pi E_\alpha (\frac{r_0}{2}(r_i - r_0)^2 + \frac{1}{3}(r_i - r_0)^3), \tag{17}$$

with E_α is the Young modulus of the M lattice site and r_i is ionic radius of the impurity. E_α is close to the bulk Young's modulus and r_0 can be computed from the length of the bonds between M and oxygen sites, and between oxygen and oxygen sites (Hiraga et al., 2004). The temperature dependency of these parameters is small and we will consider in the following $E_\alpha = 159GPa$ and $r_0 = 0.064nm$ (Hiraga et al., 2004).

Using the above expression and Eqs.2, 3 and 4 one can compute the drag pressure exerted by Cr ($r_i = 0.062nm$), Al ($r_i = 0.054nm$) and Ca ($r_i = 0.1nm$) for different grain boundary velocities and for natural characteristic c_0 concentrations of 200, 50 and $100ppm$ respectively (De Hoog et al., 2010). Considering

the diffusion coefficients of the three elements at $1573K$ (respectively, $1.4 \cdot 10^{-15}$, $1.9 \cdot 10^{-15}$, $1.9 \cdot 10^{-16}$ from (Jollands et al., 2018; Zhukova et al., 2017; Spandler et al., 2007)), we estimate that the characteristic drag pressure exerted by Ca is at least 1 order of magnitude higher than the ones exerted by Ni and Al. Thus in the following, the only impurity considered for solute drag will be Ca.

The Ca solute drag parameters α_{Ca} and β_{Ca} can be computed using equations 3 and 4 with a segregation length (δ) of $5nm$ (Hiraga et al., 2004) and an Arrhenius-type temperature dependence of the diffusion coefficient (D) where the reference value and activation energy are $D_0 = 3.16.10^{-6} mm^2.s^{-1}$ and $Q_D = 200kJ.mol^{-1}$ (Coogan et al., 2005) respectively. We obtain $\alpha_{Ca} = 3.10^7 J.S.mm^{-4}$ and $\beta_{Ca} = 9.6.10^5 s.mm^{-1}$ at 1573K and $\alpha_{Ca} = 3.10^{11} J.s.mm^{-4}$ and $\beta_{Ca} = 2.8.10^9 s.mm^{-1}$ at 1073K.

4 Laboratory and natural constraints on grain sizes in olivine-rich rocks

The main goal of this study is to show that laboratory experiments and natural observation on olivine GG can be reconciled by accounting for Ca solute drag. In the following section, we define a priori constraints on GG kinetics provided by natural and experimental data.

4.1 Laboratory constraints

The annealing experiments on ultrafine grained natural San Carlos olivine of (Karato, 1989) seem appropriate to define the experimental reference, particularly the high pressure ($300MPa$) dry runs at $1573K$. This sample has probably as much impurities as a natural mantle rock because it was synthesized using crushed grains of natural olivine, so the solute drag was probably as active in

these experiments as in nature. These experiments allow constraining grain growth kinetics for short times ($\leq 10h$) and small grain sizes ($2 - 25\mu m$).

4.2 Natural constraints

Natural constraints on GG kinetics have to be considered cautiously because of the large number of uncertainties in the determination of physical conditions of natural systems (initial size distribution, precise thermal history, pure static conditions, etc.). Contraints on thermal history, strain and grain size evolution of peridotite xenoliths can be found in the literature (e.g. (Pokhilenko et al., 2014; Baptiste and Tommasi, 2014)), but these rocks are a mixture of olivine, pyroxene and other secondary phases and their microstructural evolution is certainly affected by pinning effects due to their polymineralic nature (Furstoss et al., 2020) in addition to the solute drag effect. Nevertheless, when solely controlled by pinning, the maximum grain size is dictated by the spacing between static pinning phases like spinels (Furstoss et al., 2020) and the latter is always larger than the actual GS in natural polymineralic peridotites, like harzburgites or lherzolites (Herwegh et al., 2011). An alternative could be to focus on dunites, which are composed by $\geq 90\%$ of olivine. However, in such rocks, the initial crystal size distribution is clearly related to the mechanism of their formation, which usually involves extensive interaction with melts percolating the mantle (Berger and Vannier, 1984; Kelemen, 1990) and may be very different from the GS distribution used as initial conditions for our models. Considering these two limitations, we chose to compare our models results with classical (i.e., polymineralic) peridotites, being aware that our model only captures a part of the processes that limit the maximum grain size of natural rocks.

To focus on natural peridotites with textures typical of thermal (without stored energy) annealing according to the terminology defined by Harte (1977) we

selected examples which were described as coarse granular or protogranular. Porphyroclastic, granoblastic and tabular textures were not considered because they reflect significant rock deformation that was not subsequently fully annealed, or grain growth in presence of melts or fluids. We briefly recall here the geological setting, age and temperature history of the selected examples.

The Udachnaya (Siberia) kimberlite xenoliths

The Udachnaya kimberlite pipe in Siberia is well known due to its diamond mine and because of the occurrence of megacrystalline harzburgite and dunite xenoliths, mainly composed by coarse olivine crystals (up to 10 cm wide; (Pokhilenko et al., 2014)). The age of Udachnaya pipe has been determined between 345 and 385 Ma depending on the dating method (Dehvis et al., 1980; Ilupin et al., 1990). Equilibrium temperatures and depth of the megacrystalline peridotite xenoliths range between 1173 and 1373K and 150-200 km (Pokhilenko et al., 1993; Griffin et al., 1996). Olivine in the megacrystalline harzburgites from Udachnaya have low Ca contents (mainly $<$ 150ppm; (Pokhilenko et al., 2014)). It is impossible to determine precisely how much time they have spent at these temperatures before being extracted by the kimberlitic eruption in Late Devonian – Early Carboniferous times. Re/Os ages in diamond sulfides have provided an age for the formation of the cratonic lithosphere around 1.8 Ga (Ionov et al., 2015), if we assume that these rocks represent samples from the oldest part of the cratonic lithosphere, we can estimate a maximum residence time of these rocks at 1173-1373K of 1450 Ma. A minimum residence time is difficult to estimate, since the cratonic mantle has been modified by metasomatism (interaction with percolating melts) after its stabilization (Ionov et al., 2015).

The Kaapvaal (South Africa) kimberlite xenoliths

The Archean lithosphere of the Kaapvaal craton in South Africa stabilized

around 3 Ga ago according to Re-Os isotopic data on peridotite xenoliths (Pearson et al., 1995) extracted by kimberlite magmatism in Late Jurassic to Cretaceous times, i.e. between 180 and 90 Ma (Griffin et al., 2014). Except of the deepest sections of the lithosphere ($>$ 180km) where mylonitic microstructures and lherzolitic compositions are common, most peridotite xenoliths consist of coarse (5-8 mm) to cm-size grained harzburgites in which olivine has low intragranular deformation and rounded to polygonal shapes indicating significant annealing posterior to an early stage of deformation (e.g. (Boullier and Nicolas, 1975; Boyd and Mertzman, 1987; Baptiste and Tommasi, 2014)). Ca content in the rims of olivine grains reaches up to 1200 ppm (Hervig et al., 1986) and grain interiors have in general lower Ca content (30-600 ppm, median 100 ppm, cf. Georoc database). PT estimates range along a low geothermal gradient with temperatures of $873 - 1273K$ at depths between 80 and 150 km (Boyd et al., 1985; Chu and Korenaga, 2012; Baptiste and Tommasi, 2014). In the Jagersfontein pipe, very coarse-grained peridotite xenoliths exhibit grain sizes from 5 to 20 mm with temperature estimates ranging from $973 - 1223K$ (Winterburn et al., 1990). As precise constraints on the thermal evolution of the cratonic root are not available, in our model, we assume that the equilibrium cratonic conductive geotherm was reached rapidly after the stabilization of the cratonic lithosphere and that these rocks have spent 2 to 3 Ga at their equilibrium temperatures before being erupted. By using a mean temperature of 1173K, we obtain estimates for the olivine grain sizes at depths of 100-125km (Baptiste et al., 2015).

The Kerguelen hotspot in the Indian Ocean

The Kerguelen archipelago is part of a Large Igneous Province, the Kerguelen Plateau, formed above the Kerguelen plume (Bascou et al., 2008; Mattielli et al., 1996; Grégoire et al., 1995). Plume-related volcanism forming the Ker-

guelen Islands started around 45 Ma ago and lasted until 0.1 Ma ago ((Cottin et al., 2011) and references therein). Ultramafic xenoliths brought at the surface in the Kerguelen Islands by the plume-related volcanism are harzburgites and dunites typical of a depleted mantle which has undergone a large degree of partial melting ((Bascou et al., 2008) and references therein). Equilibrium PT conditions determined on xenoliths close to the crust-mantle boundary are around 1 GPa and 1173-1273K (Grégoire et al., 1995). Some protogranular harzburgites have mean grain sizes of 2-10 mm while equigranular dunites have a mean grain size between 0.5 and 1 mm (Bascou et al., 2008). Here again, it is difficult to estimate the annealing time of these xenoliths. Based on geochemical and petrological analyses the Kerguelen harzburgites were interpreted as residues from a partial melting episode linked with the Kerguelen plume, which were subsequently affected by melt percolation forming the dunites (Mattielli et al., 1996; Bascou et al., 2008). Peridotite xenoliths have been sampled in lavas dated between 28 and 7 Ma ((Bascou et al., 2008) and references therein) so they might have spent up to 38 Ma at temperatures close to 1173-1273K.

The temperature, rock type, mean grain size and inferred residence times for the three contexts are summarized within table 1.

Table 1: Summary of constraints on temperature, grain size and geodynamic context for the four selected peridotite samples that were used to estimate our model performance. *a* (Baptiste and Tommasi, 2014); *b* (Winterburn et al., 1990); *c* (Pokhilenko et al., 2014); *d* (Goncharov et al., 2012); *e* (Yudin et al., 2014); *f* (Grégoire et al., 1995); *g* (Bascou et al., 2008).

Region	Context	Temperature (K)	Rock type	Mean Grain size (mm)	Time (Ga)	References
Kaapvaal	Kimberlite	873 – 1273	Harzburgite	5 – 20	2 – 3	(a, b)
Siberia	Kimberlite	1173 – 1373	Harzburgite	50 – 100	0.1 – 1.5	(c, d, e)
Kerguelen	Hot Spot	1173 – 1273	Harzburgite	2 – 10	0.017 – 0.038	(f, g)
Kerguelen	Hot Spot	1173 – 1273	Dunite	0.5 – 1	0.017 – 0.038	(f, g)

The geological contexts presented above will be used in the following to test the performance of our mean-field solute drag model. In a first step, to calibrate

the solute drag parameters, we run full-field model searching for solute drag parameters that both reproduce the experimental data and predict grain sizes ranging between 0.5 and 10mm for annealing times ranging between 0.1Ma and 1Ga at a constant temperature of 1073K.

5 Results

In this section, we present the full field and mean field results for long term annealing of olivine aggregates. The olivine grain boundary energy (γ), calcium concentration within the bulk (c_0) are taken as $1 J.m^{-2}$ (Cooper and Kohlstedt, 1986) and $100 ppm$ respectively while the grain boundary mobility (M) is taken as an Arrhenius's law where the reference value and activation energy are equal to $M_0 = 4.10^4 mm^4.J^{-1}.s^{-1}$, $Q_M = 185 kJ.mol^{-1}$ (Furstoss et al., 2020) respectively.

To perform long term annealing full field simulations, passing from micrometer to millimeter scale grain sizes, we need to define a model chaining strategy. The full field simulations begin with approximately 2000 grains respecting an initial grain size distribution corresponding to the one used in laboratory experiments (Karato, 1989). When the number of grains within the simulation domain is less than 200, the simulation is stopped and a new set of 2000 grains and a larger domain is generated for the next simulation, which takes as input the final grain size distribution of the latest one. The error due to this chained calculation is minimized by sampling very precisely the final GSD and by imposing it using the Voronoï-Laguerre Dense Sphere Packing algorithm (Hitti et al., 2012).

In the following, we first propose an adjustment of the solute drag material parameters, based on full field simulations, which permits to reconcile laboratory and natural observations by producing the adequate GG kinetics. Then, the mean field model presented within section 2.2 is calibrated on the results of the

full field simulations. Finally we show an application of this framework within the geological contexts presented in section 4.2.

5.1 Full field and mean field simulations : adjustment of solute drag parameters

We begin our full field simulations using the solute drag parameters α_{Ca} and β_{Ca} presented in section 3. However at 1573K the computed GG kinetics does not match the experimental results of (Karato, 1989) (Fig.4). The predicted GG (purple curve in Fig.4) quickly deviates from the laboratory data (yellow curve); thus we stopped this simulation at the end of the second step in the model chaining strategy.

We tested different values for the solute drag parameters and found that $\alpha = 10\alpha_{Ca}$ and $\beta = 500\beta_{Ca}$ produce results consistent with laboratory results at 1573K and have GG kinetics compatible with natural observations at 1073K (Fig.4). Using those values, the mean grain size evolution begins to deviate from the classical extrapolation of laboratory results (which does not account for solute drag) for a mean grain size near $30\mu m$ at 1573K and near $50\mu m$ at 1073K (Fig.4). The GG kinetics is slowed down by solute drag for mean grain sizes of up to ca. 1mm. For coarser mean grain sizes, GG is weakly influenced by solute drag (low velocity regime in Fig.1).

The distribution of the mass term $\mathcal{M}$ (see section 2.1, Eq.11) within the simulated microstructure (Fig.5) clearly shows an increase of its value from the small grains to the large ones. At first, for ultra-fine grained aggregates as the ones used in laboratory experiments, the mass term is nearly equal to 1 within all the microstructure (Fig.5). This first phase correspond to the high velocity regime in which the grain growth kinetics is nearly unimpacted by the solute drag (Fig.1). Afterwards, as the grain sizes increase the mass term becomes

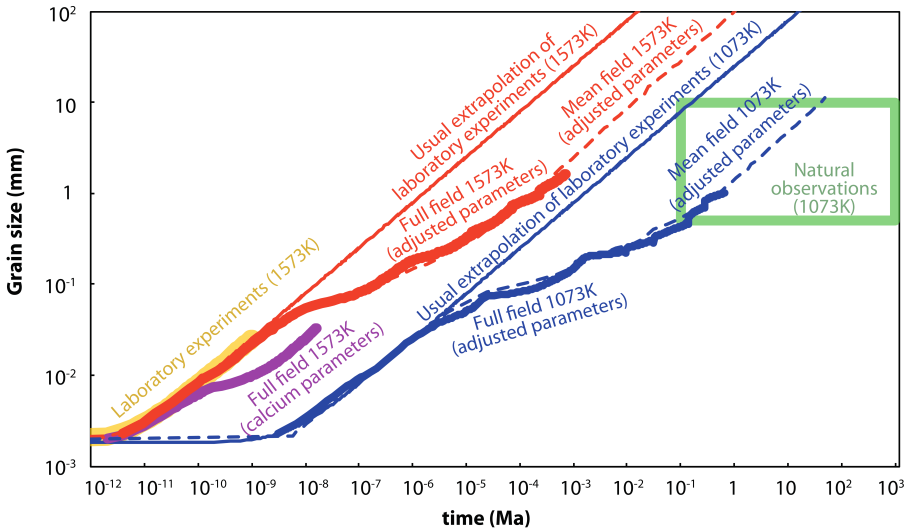

Figure 4: Olivine aggregates GG kinetics at 1573K (red) and 1073K (blue). Thin solid lines represent the usual simulations not accounting for solute drag based on the direct extrapolation of the laboratory results of (Karato, 1989) (yellow). The bold purple curve present the predictions from a full field simulation using calcium solute drag parameters α_{Ca} and β_{Ca} calculated in section 3, while the bold red and blue solid lines represent full field simulations with $\alpha = 10\alpha_{Ca}$ and $\beta = 500\beta_{Ca}$ at 1573K and 1073K, respectively . The dashed lines represent the GG kinetics computed using the mean field model with adjusted parameters based on the full field simulations at 1573K (red) and 1073K (blue). The green rectangle represents olivine mean grain sizes and annealing times typical of lithospheric mantle rocks (see section 4.2).

heterogeneously distributed between one and its maximum value depending on the local grain boundary velocities, which are controlled by the local curvature. Within this regime, the long straight grain boundary segments have higher mass terms and their velocities are near the velocity the most impacted by solute drag. Those segments are thus slowed down by solute drag. They also exert a pinning force on other grain boundaries, which enhances the deceleration of the grain growth kinetics. Finally, when grain sizes are sufficiently large, the grain boundary velocities become very small and one enters the low velocity regime in which

the grain growth kinetics is again weakly impacted by the solute drag (Fig.1). The mass term reaches almost its maximum value in the whole microstructure (Fig.5). However, locally, smaller grains, which may correspond to those being consumed in the annealing process, have lower mass terms and intermediate velocities, closer to the one most impacted by solute drag. Migration of these boundaries is slowed down by solute drag and this affects the whole system. Thus, in the low velocity regime, solute drag has a weaker, but non-negligible effect on the average grain growth velocity.

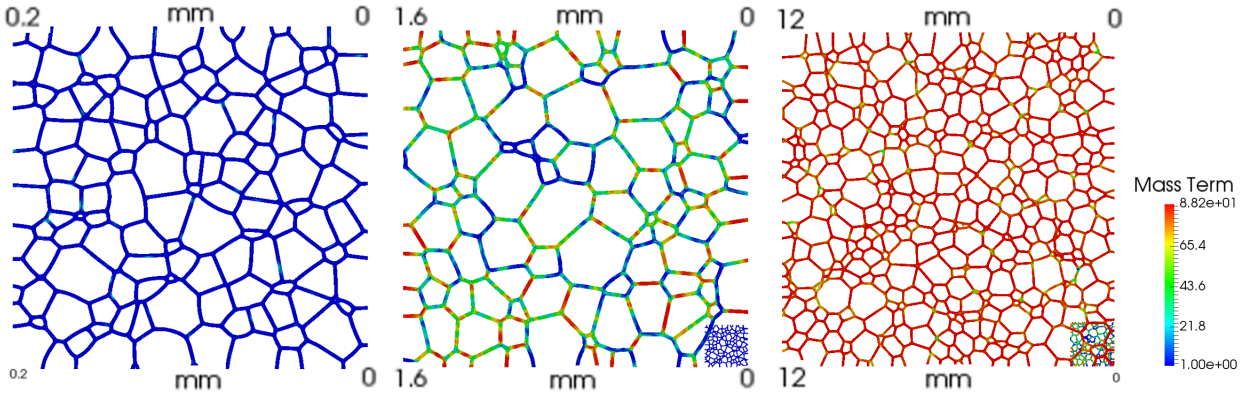

Figure 5: Distribution of mass term $\mathcal{M}$ along grain boundaries for the first three runs at 1573K using $\alpha = 10\alpha_{Ca}$ and $\beta = 500\beta_{Ca}$. The first run (left), a $0.2mm$ aside square, is also represented in the right bottom corner of the second run (center), a $1.6mm$ aside square, which is also represented at the right bottom corner of the third run (right), a $12mm$ aside square.

The analysis of the GG kinetics for simulations with different initial mean grain sizes highlights a first phase of very slow or even null mean grain size evolution (Fig.6). For the equivalent full field models without accounting for the solute drag, this first phase of very slow GG also exists but is much shorter than for the models accounting for solute drag (Fig.6). The full field simulations, which explicitly consider solute drag predict that the initial grain size does not affect GG kinetics apart from delaying the start of the rapid GG stage. The

duration of this phase of slow GG is longer when the initial mean grain size is coarse (Fig.6). This initial slow GG kinetics can be explained by analyzing the GSD (Fig.7). In fact, when the initial microstructure is composed of coarse grains, some grains have to shrink to let the other ones grow. This can be seen by comparing in Fig.7a the GSD of the initial microstructure and that at the end of the initial slow GG phase for the experiment with the coarser initial mean grain size in Fig.6. This comparison highlights an enrichment in small grains (Fig.7a). Before disappearing, the GBM velocities of the shrinking grains will necessarily pass through a velocity regime highly impacted by the presence of impurities. This will affect the grain growth kinetics directly (by slowing down the shrinking) and indirectly by impeding the movements of the other grain boundaries through pinning mechanisms.

After calibration, the mean field model (Eq.16) reproduces correctly the full field modeled GG kinetics for both temperatures (Figs.4 and 6). The best fitting mean field parameters C_α, C_β and n are equal to 0.7, 0.25 and 0.15 respectively. The GSD predicted by the mean field approach is consistent with the full field modeled ones (Fig.7) but some differences appear for long annealing times (Fig.7b). However these differences between full field and mean field predicted GSD after long annealing times seem to do not strongly impact the mean grain size predictions since the mean field simulations are in good agreement with the full field calculations, in terms of mean grain size, even for long annealing times (Figs.4 and 6). This mean field approach allows to be predictive on olivine aggregates GG kinetics for a much lower computational cost, which permits to test our formalism on different geological contexts.

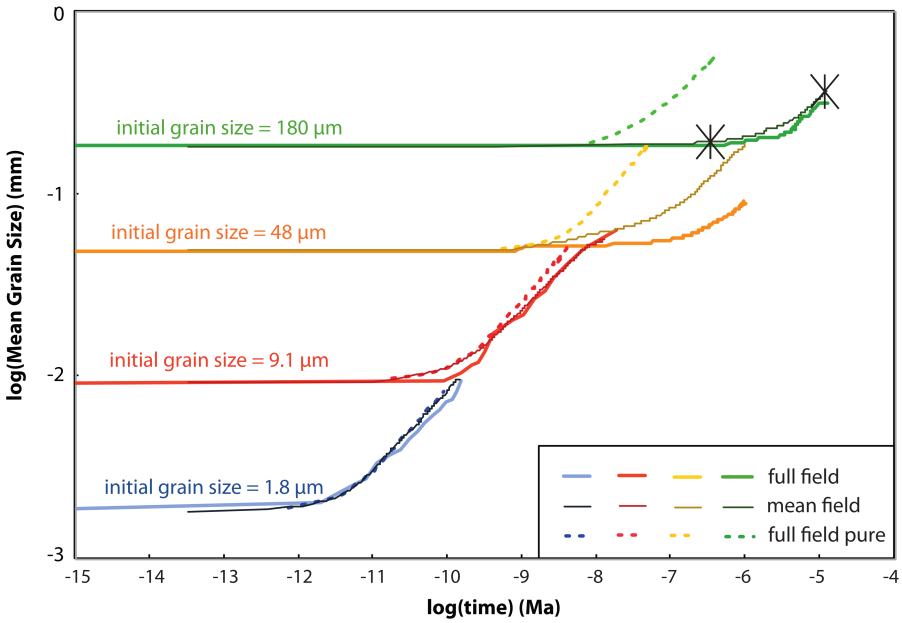

Figure 6: Mean grain size evolution at 1573K for $\alpha = 10\alpha_{Ca}$ and $\beta = 500\beta_{Ca}$ for the first four steps of the simulation (without the time offset normally applied to get the whole grain growth kinetics presented in Fig.4), the full large lines represent the full field model accounting for impurity, the full tiny lines represent the mean field computations and the dashed lines represent the equivalent full field models without impurity. The black stars represent the two sampling points for the GSD presented in Fig.7.

5.2 Implication for the microstructural evolutions in ultramafic rocks

To estimate how well our mean field model predicts the average grain size of natural samples with reasonable c_0 (Ca concentration within bulk) values, we test it against different contexts in terms of annealing temperature and measured grain sizes.

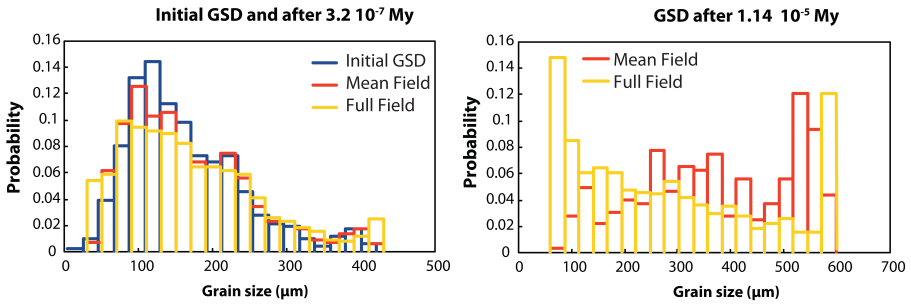

(a) (b)

Figure 7: GSD (in number) for the fourth run presented in figure 6 (the green one, at 1573K for $\alpha = 10\alpha_{Ca}$ and $\beta = 500\beta_{Ca}$), 7a : initial GSD (blue), mean field (orange) and full field (yellow) modeled GSD after $10^7 s$, 7b : mean field (orange) and full field (yellow) modeled GSD after $3.6.10^8 s$.

5.2.1 Mean field GG models

For the mean field GG model, the temperature is kept constant and grain size grows indefinitely; we compute the GG curve for residence times up to 2 Ga. GG curves are computed from four temperatures of 1073, 1173, 1273 and 1373K and c_0 values of 600, 800, 1000 and 1200 ppm.

All models were run initially with an initial grain size of $20\mu m$ and a standard deviation of $2\mu m$; then, isothermal models were run again with an initial grain size of 0.5mm and a standard deviation of $50\mu m$ and an intial grain size of 2mm and a standard deviation of $200\mu m$. In fact, the initial grain size has no effect of the grain growth curve or final grain size, apart from shifting the beginning of the positive slope on the grain growth curve (Fig.8).

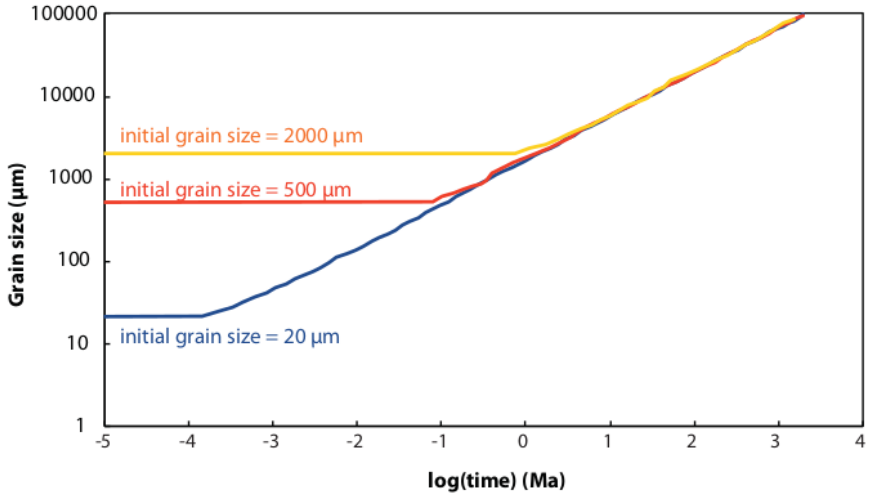

Figure 8: Grain size evolution for isothermal model with $T = 1173K$, $c_0 = 800ppm$ and three initial grain sizes of 20, 500 and $2000\mu m$.

5.2.2 Results

The c_0 parameter, in the range of tested values, has only a moderate effect of the final or intermediate grain sizes (table 2 and figure 9). In all simulations in which solute drag is considered grain sizes are considerably smaller than the ones predicted in simulations without impurities. In such simulations, for isothermal conditions, grain sizes reach 2 and 8 meters after 1 Ga at temperatures of 1173 and 1373K, respectively, while they do not exceed 47 cm for the solute drag simulation with the largest temperature (1373K) and the lowest impurity concentration (600 ppm).

Mean field models predict a GG rate which decreases exponentially with time (Fig.9). Extremely large grain sizes of several cm can be reached for conditions (temperature and annealing times) consistent with those inferred for the Udachnaya kimberlite xenoliths (i.e., temperatures between 1173 to 1273K and residence times between 100 and 1450 Ma). The Kaapvaal peridotites,

which have smaller grain sizes and potentially larger residence times than the Udachnaya ones, range below the 1073K temperature curve. Thus, if the annealing times of these peridotites are, as inferred, $> 1Ga$ their grain sizes cannot therefore be explained by solute drag only, even if the predictions of the simulations with solute drag are closer to the observed values.

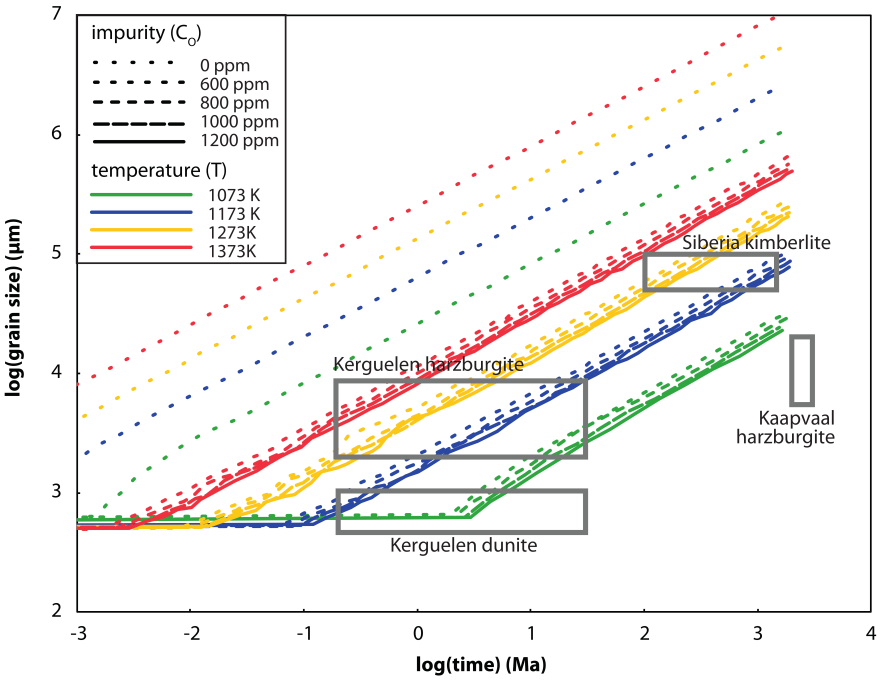

Figure 9: Grain size evolution for isothermal models with 4 different temperatures and 4 different impurity (c_0) concentrations. Solid squares indicate the approximate location of Siberia and Kerguelen and Kaapvaal xenoliths on this curve according to the literature (see references in Tab.1).

Table 2: Temperature and impurity concentrations (c_0) conditions for the mean field simulations and their results in terms of grain sizes at two different steps (10 and 1000 Ma).

Temperature (K)	C0 (ppm)	Grain Size (mm)	
		10Ma	1000Ma
1073	600	2.1	24
1073	800	1.7	21
1073	1000	1.6	18
1073	1200	1.3	17
1173	600	7	74
1173	800	5.9	68
1173	1000	5.1	58
1173	1200	4.9	55
1273	600	17	209
1273	800	14	180
1273	1000	13	161
1273	1200	12	45
1373	600	41	470
1373	800	36	392
1373	1000	31	360
1373	1200	29	343

Olivine grain sizes measured in the Kerguelen harzburgites (2-10 mm) may be simulated if annealing times at temperatures >1373K are smaller than 1Ma. They are consistent with up to 38Ma of annealing at temperature $\leq$ 1173K. The smaller olivine grain sizes in the Kerguelen dunites may only be explained by lower equilibration temperatures and annealing times (very short annealing at 1173K or up to 10Ma of annealing at 1073K).

6 Discussion

GG simulations, which explicitly consider solute drag by Ca impurities in olivine, adequately reproduce both grain size evolution in laboratory experiments and observed grain size ranges in mantle peridotites subjected to various annealing times in the lithospheric mantle, if solute drag parameters derived directly from theoretical considerations on the interactions between Ca impurities and olivine grain boundaries, in particular β, are increased by two orders of magnitude. This difference could arise from two main reasons :

First, the two functions $D(x)$ and $E(x)$ (diffusion coefficient and interaction energy as function of distance to grain boundary x) needed for the calculation of solute drag parameters α and β (see section 2) are poorly known even for metallic materials in which the interaction between an impurity ion and a grain boundary is mostly elastic. For ceramics-like materials such as olivine, this interaction should also account for electrostatic interaction between the solute ion and the grain boundary and the interaction between solute-vacancy dipoles and electrical field around grain boundaries (Yan et al., 1983). The quantification of all of those interactions should be done by atomistic calculations using systematic approaches for describing grain boundaries (e.g. (Hirel et al., 2019)) and their interactions with solute.

Secondly, it is well accepted that the impurity concentration at grain boundary evolves with the grain size, increasing when grain size increases (Marquardt and Faul, 2018) which could also be expressed by a grain size dependent partition coefficient (Hiraga et al., 2004). Even if the solute drag pressure (Eq.2) depends on grain matrix impurity concentration, one can find expressions for α and β as functions of the partition coefficient (Cahn, 1962). The effect of indirectly introducing an increase in the grain boundary impurity concentration with increasing grain size may be similar to an increase of β, as we did here. In fact, increasing

the β value will increase the space of the high velocity regime for which the grain boundary migration will be poorly affected by impurities. An increase of the impurity concentration with grain size will also result in a lower impact of the solute drag for small grains. Moreover, it will also increase the domain of effect of solute drag and decrease GG rates of coarse grained polycrystals.

Our full field and mean field simulations show an initial phase of very slow grain size evolution (Figs.6 and 8) due to the direct slow down of the grain shrinkage and growth by solute drag, and indirectly by the impediment of GBM by the impurity slowed grain boundaries. This quasi-static phase, which is longer for coarser initial grain sizes, implies a very weak dependency of the grain growth kinetics on initial grain size. This small dependency frees us from the need of precise constrains on the initial grain size, which is very difficult to know in geological contexts. Taking advantage of this, we can apply our solute drag model for different stable geological contexts. For the majority of the geological contexts presented here, our formalism shows consistent grain size / time predictions (Fig.9). It is difficult to evaluate precisely the performance of our models with respect to the evolution of natural samples, given the lack of data concerning their temperature and grain size evolution. However, impurity drag due to Ca concentration in olivine, in the range of commonly observed value, explains a grain size reduction of several orders of magnitude at geological timescales, compared to models without impurities.

In the simulations presented in this work, secondary phases are not taken into account, which could explain why some of our simulations applied to geological contexts overestimated grain sizes (particularly for Kaapvaal harzburgites, cf Fig.9). Indeed, the presence of secondary phases such as pyroxenes and alumina phases in natural rocks is known to both impose, through Smith-Zener pinning mechanisms, a maximal grain size (Tasaka et al., 2014; Nakakoji et al.,

2018) (i.e. distance between second phase grains) and to reduce grain growth kinetics (Furstoss et al., 2020) of the rocks. In natural annealed peridotites, the distance and the size of second phase grains range between few mm to few cm. This distance constrains the maximum mean grain size that may be attained in a polyphasic rock, making predictions of grain sizes of tens of cm and higher unrealistic. Other natural factors could also be taken into consideration for a holistic description of the mechanisms impacting grain growth. For example, it has been shown that the presence of melt and the water content in the material impact the GG within laboratory experiments by accelerating the growth kinetics (Evans et al., 2001). This effect may be similar in a geological context in which metasomatism has been active and/or melt has percolated within the rock and/or water content is high.

7 Conclusions

In this work we have demonstrated that accounting for the presence of impurities within olivine rich-rocks permits to explain GG kinetics of both experimentally and naturally annealed olivine aggregates. The solute drag parameters in the simulations that allow for fitting both datasets are however quite different from those predicted for Ca, which is the impurity expected to have the highest impact on olivine grain boundary migration in mantle rocks, based on simple theoretical considerations. Atomistic calculations or a new experimental framework are needed to explain this gap.

We have developed a new mean field model accounting for the presence of those impurities and showed this approach could be used to predict grain size of olivine-rich rocks in geological contexts such as isothermal evolution. As this approach successfully reproduced natural grain size in annealed peridotite, healing kinetics may be implemented in large scale numerical geodynamic models

based on this framework. In order to have a useful grain size evolution law for geodynamic model, a model accounting for the competition between grain size reduction due to deformation (through dynamic recrystallization phenomenon) and growth should be developed.

This approach is fast enough for implementation in large scale numerical geodynamic models and allows for better predictions of olivine grain sizes than the direct extrapolation of the experimentally-derived flow laws. However, to be consistent with the real multiphase nature of natural rocks, the influence of second phases, such as pyroxenes and Al-rich phases, on GG kinetics should also be considered. The present work shows that the latter plays in particular a major role in limiting the maximum grain size that may be achieved, whereas solute drag plays a very important role in the initial stages of the growth process, when olivine grain sizes are smaller than the second phase spacing. Such a framework may open the door to a paleo-chronometer based on grain size evolution in geological contexts where deformation has stopped and static GG predominates.

8 Acknowledgments

We greatly acknowledge Editor Juan Carlos Afonso and the two anonymous reviewers for their constructive comments.

This work was supported by CNRS INSU 2018-programme TelluS-SYSTER.

The support of the French Agence Nationale de la Recherche (ANR), Arcelor-Mittal, FRAMATOME, ASCOMETAL, AUBERT&DUVAL, CEA, SAFRAN through the DIGIMU Industrial Chair and consortium are gratefully acknowledged.

9 Data availability

The data for supporting all figures of the paper are avalaible upon request to the authors as well as the mean field code used in this work.

References

Baptiste, V. and Tommasi, A. (2014). Petrophysical constraints on the seismic properties of the kaapvaal craton mantle root. *Solid Earth*, 5(1):45.

Baptiste, V., Tommasi, A., Vauchez, A., Demouchy, S., and Rudnick, R. L. (2015). Deformation, hydration, and anisotropy of the lithospheric mantle in an active rift: constraints from mantle xenoliths from the north tanzanian divergence of the east african rift. *Tectonophysics*, 639:34–55.

Bascou, J., Delpech, G., Vauchez, A., Moine, B., Cottin, J.-Y., and Barruol, G. (2008). An integrated study of microstructural, geochemical, and seismic properties of the lithospheric mantle above the kerguelen plume (indian ocean). *Geochemistry, Geophysics, Geosystems*, 9(4).

Bercovici, D. and Ricard, Y. (2012). Mechanisms for the generation of plate tectonics by two-phase grain-damage and pinning. *Physics of the Earth and Planetary Interiors*, 202:27–55.

Bercovici, D. and Ricard, Y. (2014). Plate tectonics, damage and inheritance. *Nature*, 508(7497):513.

Berger, E. and Vannier, M. (1984). Les dunites en enclaves dans les basaltes alcalins des îles océaniques: approche pétrologique. *Bulletin de minéralogie*, 107(5):649–663.

Bernacki, M., Logé, R. E., and Coupez, T. (2011). Level set framework for the finite-element modelling of recrystallization and grain growth in polycrystalline materials. *Scripta Materialia*, 64(6):525–528.

Bernacki, M., Resk, H., Coupez, T., and Logé, R. E. (2009). Finite element model of primary recrystallization in polycrystalline aggregates using a level set framework. *Modelling and Simulation in Materials Science and Engineering*, 17(6):064006.

Boullier, A. M. and Nicolas, A. (1975). Classification of textures and fabrics of peridotite xenoliths from south african kimberlites. In *Physics and Chemistry of the Earth*, pages 467–475. Elsevier.

Boyd, F., Gurney, J., and Richardson, S. (1985). Evidence for a 150–200-km thick archaean lithosphere from diamond inclusion thermobarometry. *Nature*, 315(6018):387–389.

Boyd, F. and Mertzman, S. (1987). Composition and structure of the kaapvaal lithosphere, southern africa. In *Magmatic processes: physicochemical principles*, volume 1, pages 13–24. The Geochemical Society.

Braun, J., Chéry, J., Poliakov, A., Mainprice, D., Vauchez, A., Tomassi, A., and Daignières, M. (1999). A simple parameterization of strain localization in the ductile regime due to grain size reduction: A case study for olivine. *Journal of Geophysical Research: Solid Earth*, 104(B11):25167–25181.

Cahn, J. W. (1962). The impurity-drag effect in grain boundary motion. *Acta metallurgica*, 10(9):789–798.

Chu, X. and Korenaga, J. (2012). Olivine rheology, shear stress, and grain growth in the lithospheric mantle: geological constraints from the kaapvaal craton. *Earth and Planetary Science Letters*, 333:52–62.

Coogan, L., Hain, A., Stahl, S., and Chakraborty, S. (2005). Experimental determination of the diffusion coefficient for calcium in olivine between 900 c and 1500 c. *Geochimica et Cosmochimica Acta*, 69(14):3683–3694.

Cooper, R. and Kohlstedt, D. (1986). Rheology and structure of olivine-basalt partial melts. *Journal of Geophysical Research: Solid Earth*, 91(B9):9315–9323.

Cottin, J.-Y., MiChon, G., and DelpeCh, G. (2011). The kerguelen volcanic plateau: the second largest oceanic igneous province (lip) on earth and a witness of the indian ocean opening. *The Kerguelen Plateau: Marine Ecosystems and Fisheries*, 2011:29–42.

Cottrell, A. H. and Bilby, B. (1949). Dislocation theory of yielding and strain ageing of iron. *Proceedings of the Physical Society. Section A*, 62(1):49.

Cruz-Fabiano, A. L., Logé, R., and Bernacki, M. (2014). Assessment of simplified 2d grain growth models from numerical experiments based on a level set framework. *Computational Materials Science*, 92:305–312.

De Hoog, J. C., Gall, L., and Cornell, D. H. (2010). Trace-element geochemistry of mantle olivine and application to mantle petrogenesis and geothermobarometry. *Chemical Geology*, 270(1-4):196–215.

Dehvis, G., Sobolev, N., and Khar'kiv, A. (1980). New data on the age of yakutian kimberlites obtained by uranium-lead study of zircons. *Doklady Akademii Nauk SSSR*, 254(1):175–179.

Evans, B., Renner, J., and Hirth, G. (2001). A few remarks on the kinetics of static grain growth in rocks. *International Journal of Earth Sciences*, 90(1):88–103.

Florez, S., Shakoor, M., Toulorge, T., and Bernacki, M. (2020). A new finite element strategy to simulate microstructural evolutions. *Computational Materials Science*, 172:109335.

Furstoss, J., Bernacki, M., Ganino, C., Petit, C., and Pino-Muñoz, D. (2018). 2d and 3d simulation of grain growth in olivine aggregates using a full field model based on the level set method. *Physics of the Earth and Planetary Interiors*, 283:98–109.

Furstoss, J., Bernacki, M., Petit, C., Fausty, J., Pino-Muñoz, D., and Ganino, C. (2020). Full field and mean field modeling of grain growth in a multiphase material under dry conditions: application to peridotites. *Journal of Geophysical Research: Solid Earth*, page e53942.

Goncharov, A., Ionov, D., Doucet, L. S., and Pokhilenko, L. (2012). Thermal state, oxygen fugacity and c o h fluid speciation in cratonic lithospheric mantle: New data on peridotite xenoliths from the udachnaya kimberlite, siberia. *Earth and Planetary Science Letters*, 357:99–110.

Grégoire, M., Cottin, J.-Y., Mattielli, N., Nicollet, C., Weis, D., and Giret, A. (1995). The kerguelen archipelago: an hypothetic continental mafic protolith. *Terra Antarctica*, 2(1):1ą6.

Griffin, W., Batumike, J., Greau, Y., Pearson, N., Shee, S., and O'Reilly, S. Y. (2014). Emplacement ages and sources of kimberlites and related rocks in southern africa: U–pb ages and sr–nd isotopes of groundmass perovskite. *Contributions to Mineralogy and Petrology*, 168(1):1032.

Griffin, W., Kaminsky, F., Ryan, C., O'Reilly, S., Win, T., and Ilupin, I. (1996). Thermal state and composition of the lithospheric mantle beneath the daldyn kimberlite field, yakutia. *Tectonophysics*, 262(1-4):19–33.

Guillope, M. and Poirier, J. (1979). Dynamic recrystallization during creep of single-crystalline halite: An experimental study. *Journal of Geophysical Research: Solid Earth*, 84(B10):5557–5567.

Harte, B. (1977). Rock nomenclature with particular relation to deformation and recrystallisation textures in olivine-bearing xenoliths. *The Journal of Geology*, 85(3):279–288.

Hervig, R., Smith, J., and Dawson, J. (1986). Lherzolite xenoliths in kimberlites and basalts: petrogenetic and crystallochemical significance of some minor and trace elements in olivine, pyroxenes, garnet and spinel. *Earth and Environmental Science Transactions of the Royal Society of Edinburgh*, 77(3):181–201.

Herwegh, M., Linckens, J., Ebert, A., Berger, A., and Brodhag, S. (2011). The role of second phases for controlling microstructural evolution in polymineralic rocks: A review. *Journal of Structural Geology*, 33(12):1728–1750.

Hillert, M. (1965). On the theory of normal and abnormal grain growth. *Acta metallurgica*, 13(3):227–238.

Hiraga, T., Anderson, I. M., and Kohlstedt, D. L. (2003). Chemistry of grain boundaries in mantle rocks. *American Mineralogist*, 88(7):1015–1019.

Hiraga, T., Anderson, I. M., and Kohlstedt, D. L. (2004). Grain boundaries as reservoirs of incompatible elements in the earth's mantle. *Nature*, 427(6976):699.

Hiraga, T., Tachibana, C., Ohashi, N., and Sano, S. (2010). Grain growth systematics for forsterite±enstatite aggregates: Effect of lithology on grain size in the upper mantle. *Earth and Planetary Science Letters*, 291(1-4):10–20.

Hirel, P., Moladje, G. F. B., Carrez, P., and Cordier, P. (2019). Systematic theoretical study of [001] symmetric tilt grain boundaries in mgo from 0 to 120 gpa. *Physics and Chemistry of Minerals*, 46(1):37–49.

Hitti, K., Laure, P., Coupez, T., Silva, L., and Bernacki, M. (2012). Precise generation of complex statistical representative volume elements (rves) in a finite element context. *Computational Materials Science*, 61:224–238.

Humphreys, F. J. and Hatherly, M. (2012). *Recrystallization and related annealing phenomena*. Elsevier.

Ilupin, I., Vaganov, V., and Prokopchuk, B. (1990). Kimberlites. *Moscow, Nedra.[In Russian.]*.

Ionov, D. A., Carlson, R. W., Doucet, L. S., Golovin, A. V., and Oleinikov, O. B. (2015). The age and history of the lithospheric mantle of the siberian craton: Re–os and pge study of peridotite xenoliths from the obnazhennaya kimberlite. *Earth and Planetary Science Letters*, 428:108–119.

Jollands, M., O'Neill, H. S. C., Van Orman, J., Berry, A., Hermann, J., Newville, M., and Lanzirotti, A. (2018). Substitution and diffusion of cr2+ and cr3+ in synthetic forsterite and natural olivine at 1200–1500 c and 1 bar. *Geochimica et cosmochimica acta*, 220:407–428.

Karato, S. (1989). Grain growth kinetics in olivine aggregates. *Tectonophysics*, 168(4):255–273.

Karato, S.-I., Paterson, M. S., and FitzGerald, J. D. (1986). Rheology of synthetic olivine aggregates: influence of grain size and water. *Journal of Geophysical Research: Solid Earth*, 91(B8):8151–8176.

Kelemen, P. B. (1990). Reaction between ultramafic rock and fractionating

basaltic magma i. phase relations, the origin of calc-alkaline magma series, and the formation of discordant dunite. *Journal of petrology*, 31(1):51–98.

Lücke, K. and Detert, K. (1957). A quantitative theory of grain-boundary motion and recrystallization in metals in the presence of impurities. *Acta Metallurgica*, 5(11):628–637.

Maire, L., Scholtes, B., Moussa, C., Bozzolo, N., Muñoz, D. P., and Bernacki, M. (2016). Improvement of 3d mean field models for capillarity-driven grain growth based on full field simulations. *Journal of materials science*, 51(24):10970–10981.

Maire, L., Scholtes, B., Moussa, C., Bozzolo, N., Muñoz, D. P., Settefrati, A., and Bernacki, M. (2017). Modeling of dynamic and post-dynamic recrystallization by coupling a full field approach to phenomenological laws. *Materials & Design*, 133:498–519.

Marquardt, K. and Faul, U. H. (2018). The structure and composition of olivine grain boundaries: 40 years of studies, status and current developments. *Physics and Chemistry of Minerals*, 45(2):139–172.

Mattielli, N., Weis, D., Grégoire, M., Mennessier, J. P., Cottin, J.-Y., and Giret, A. (1996). Kerguelen basic and ultrabasic xenoliths: evidence for long-lived kerguelen hotspot activity. *Lithos*, 37(2-3):261–280.

Nakakoji, T. and Hiraga, T. (2018). Diffusion creep and grain growth in forsterite+ 20 vol% enstatite aggregates: 2. their common diffusional mechanism and its consequence for weak-temperature-dependent viscosity. *Journal of Geophysical Research: Solid Earth*, 123(11):9513–9527.

Nakakoji, T., Hiraga, T., Nagao, H., Ito, S., and Kano, M. (2018). Diffusion creep and grain growth in forsterite+ 20 vol% enstatite aggregates: 1.

high-resolution experiments and their data analyses. *Journal of Geophysical Research: Solid Earth*, 123(11):9486–9512.

Ohuchi, T. and Nakamura, M. (2007). Grain growth in the forsterite–diopside system. *Physics of the Earth and Planetary Interiors*, 160(1):1–21.

Osher, S. and Sethian, J. A. (1988). Fronts propagating with curvature-dependent speed: algorithms based on hamilton-jacobi formulations. *Journal of computational physics*, 79(1):12–49.

Pearson, D., Shirey, S., Carlson, R., Boyd, F. R., Pokhilenko, N., and Shimizu, N. (1995). Re/os, sm/nd, and rb/sr isotope evidence for thick archaean lithospheric mantle beneath the siberian craton modified by multistage metasomatism. *Geochimica et Cosmochimica Acta*, 59(5):959–977.

Pokhilenko, L., Mal'Kovets, V., Kuz'Min, D., and Pokhilenko, N. (2014). New data on the mineralogy of megacrystalline pyrope peridotite from the udachnaya kimberlite pipe, siberian craton, yakutian diamondiferous province. In *Doklady Earth Sciences*, volume 454, page 179. Springer Science & Business Media.

Pokhilenko, N., Sobolev, N., Boyd, F., Pearson, D., and Shimizu, N. (1993). Megacrystalline pyrope peridotites in the lithosphere of the siberian platform: mineralogy, geochemical peculiarities and the problem of their origin. *Russian Geology and Geophysics*, 34:56–67.

Resk, H., Delannay, L., Bernacki, M., Coupez, T., and Logé, R. (2009). Adaptive mesh refinement and automatic remeshing in crystal plasticity finite element simulations. *Modelling and Simulation in Materials Science and Engineering*, 17(7):075012.

Scholtes, B., Boulais-Sinou, R., Settefrati, A., Muñoz, D. P., Poitrault, I., Montouchet, A., Bozzolo, N., and Bernacki, M. (2016). 3d level set modeling of static recrystallization considering stored energy fields. *Computational Materials Science*, 122:57–71.

Scholtes, B., Shakoor, M., Settefrati, A., Bouchard, P.-O., Bozzolo, N., and Bernacki, M. (2015). New finite element developments for the full field modeling of microstructural evolutions using the level-set method. *Computational Materials Science*, 109:388–398.

Shakoor, M., Scholtes, B., Bouchard, P.-O., and Bernacki, M. (2015). An efficient and parallel level set reinitialization method–application to micromechanics and microstructural evolutions. *Applied Mathematical Modelling*, 39(23-24):7291–7302.

Skemer, P. and Karato, S.-i. (2007). Effects of solute segregation on the grain-growth kinetics of orthopyroxene with implications for the deformation of the upper mantle. *Physics of the Earth and Planetary Interiors*, 164(3-4):186–196.

Spandler, C., O'Neill, H. S. C., and Kamenetsky, V. S. (2007). Survival times of anomalous melt inclusions from element diffusion in olivine and chromite. *Nature*, 447(7142):303.

Suzuki, K. (1987). Grain-boundary enrichment of incompatible elements in some mantle peridotites. *Chemical Geology*, 63(3-4):319–334.

Tasaka, M., Hiraga, T., and Michibayashi, K. (2014). Influence of mineral fraction on the rheological properties of forsterite+ enstatite during grain size sensitive creep: 3. application of grain growth and flow laws on peridotite ultramylonite. *Journal of Geophysical Research: Solid Earth*, 119(2):840–857.

Vissers, R., Drury, M., Strating, E. H., and Wal, D. v. d. (1991). Shear zones

in the upper mantle: A case study in an alpine iherzolite massif. *Geology*, 19(10):990–993.

Winterburn, P. A., Harte, B., and Gurney, J. J. (1990). Peridotite xenoliths from the jagersfontein kimberlite pipe: I. primary and primary-metasomatic mineralogy. *Geochimica et Cosmochimica Acta*, 54(2):329–341.

Yan, M., Cannon, R., and Bowen, H. (1983). Space charge, elastic field, and dipole contributions to equilibrium solute segregation at interfaces. *Journal of Applied Physics*, 54(2):764–778.

Yudin, D., Tomilenko, A., Travin, A., Agashev, A., Pokhilenko, N., and Orihashi, Y. (2014). The age of udachnaya-east kimberlite: U/pb and 40 ar/39 ar data. In *Doklady Earth Sciences*, volume 455, pages 288–290. Pleiades Publishing.

Zhukova, I., O'Neill, H., and Campbell, I. H. (2017). A subsidiary fast-diffusing substitution mechanism of al in forsterite investigated using diffusion experiments under controlled thermodynamic conditions. *Contributions to Mineralogy and Petrology*, 172(7):53.